JOURNAL OF MATERIALS SCIENCE 22 (1987) 4221–4232

The discontinuous precipitation of $M_{23}C_6$ in Nimonic 80A

W. E. VOICE, R. G. FAULKNER
Department of Materials Engineering and Design, Loughborough University of Technology, Loughborough, Leicestershire LE11 3TU, UK

An important distinction is made between the discontinuous precipitation of $M_{23}C_6$ carbide (where M = metal) in a nickel-base superalloy compared with those in other systems. The reaction is considered pseudo-discontinuous since carbon must diffuse to the precipitate from the general matrix. The additional factor imposed by the partial carbon-diffusion controlled growth is utilized to uniquely define the kinetics of the discontinuous precipitation. This paper details the theory involved and then compares the computed results with extensive measurements made in a transmission electron microscope of precipitates in Nimonic 80A. The results show the feasibility of the participation of carbon-diffusion control in growth. They also confirm the high dependence of discontinuous precipitation on grain-boundary nucleation and on the direction of growth in the receding grain. The theoretical analysis is used to indicate how discontinuous precipitation may be avoided by heat treatment and compositional control.

1. Introduction

The many existing theories of discontinuous precipitation [1] in a wide range of alloys systems have been well documented in the recent review papers by Gust [2] and Williams and Butler [3]. An important distinction should be made, however, for the discontinuous precipitation of $M_{23}C_6$ carbide (where M = metal) in nickel-base superalloys, since carbon must diffuse to the precipitate from a relatively large distance. The reaction is therefore only partly discontinuous and its kinetics deviate from those normally accepted because carbon depletion must occur. This phenomenon imposes a further growth factor which has been utilized to uniquely define precipitation without resort to free-energy considerations, which are difficult to evaluate in practice.

Cells of discontinuous $M_{23}C_6$ precipitates form at grain boundaries in Nimonic 80A, such as shown in Fig. 1a. A cell consists of a series of aligned $M_{23}C_6$ carbide rods (M mainly chromium) within a nickel solid solution matrix. These fcc phases have lattice parameters in an approximate ratio of 3 : 1 and have a crystallographic orientation relationship with each other and the host grain. Growth is by advancement of the grain/cell boundary into the differently oriented grain, leaving behind solute-depleted matrix and an array of carbide rods aligned perpendicularly to the advancing boundary.

2. Proposed theory of discontinuous growth

2.1. Growth mechanism

A simplistic view of discontinuous precipitation is taken. Experimental observations such as in Fig. 1a show the cell to grow by a planar advance from the original grain boundary as depicted in Fig. 1b. The distortion at the edge of the cell is over a relatively short distance so that in most cases the centre of the observed cell section is representative of the whole cell. In this region, the supply of interstitial carbon diffusing to the boundary from the matrix α' is matched by that of the substitutional solute M diffusing along the boundary.

The discontinuous cell growth is initiated when nucleation of $M_{23}C_6$ on the boundary is complete. This is when the solute catchment areas of the established nuclei have covered the boundary so that further nucleation is prevented. Discontinuous precipitation then occurs by the migration of the grain boundary into the differently oriented grain. During the transfer of atoms from this receding grain to the cell, M-solute is channelled along the boundary to the rod-shaped precipitates of $M_{23}C_6$ which grow perpendicular to the cell boundary. The matrix α separating these precipitates is therefore depleted in solute.

Precipitate rods within the cell are treated individually. Single rods compete with neighbouring rods to collect M-solute from the boundary. Where the M-solute catchment areas meet, the M-concentration within the boundary is assumed equal to that of the matrix in the receding grain. As growth rate decreases these areas are extended, resulting in a continual reduction in rod density.

The next two parts of this section discuss the analytical equations necessary to describe (i) grain-boundary migration and precipitate rod lengthening rate, and (ii) precipitate rod diameter during cell growth.

In practice the overall cell growth is dictated by a combination of the above two processes, and the balance of the contributions of both processes is determined by the boundary velocity. This situation of

0022–2461/87 $03.00 + .12

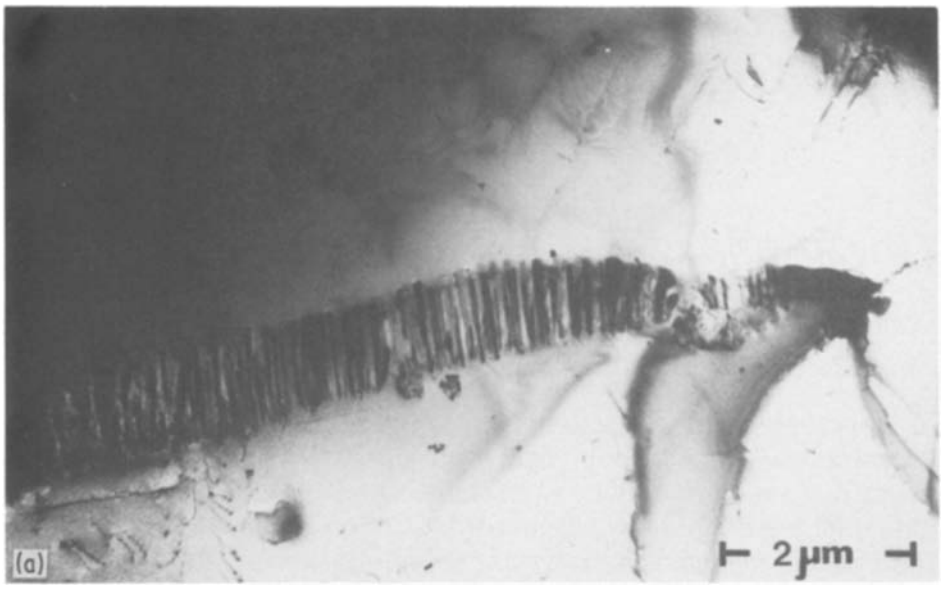

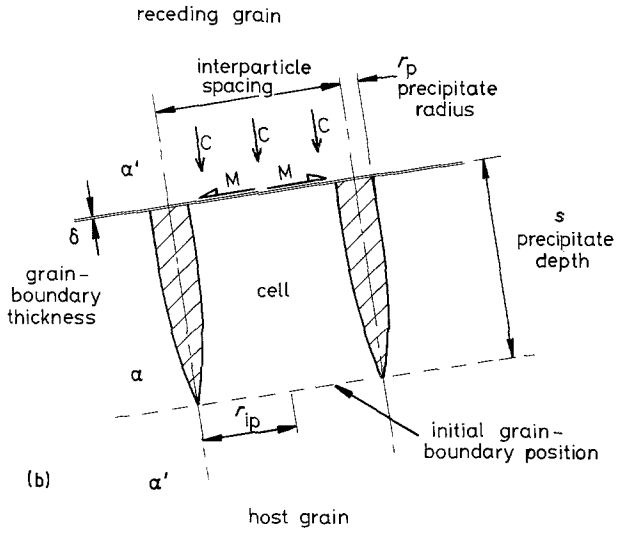

Figure 1 (a) Transmission electron micrograph of typical discontinuous precipitate in Nimonic 80A. (b) Schematic diagram of discontinuous precipitation. α and α' indicate solute depleted and supersaturated solid solution, respectively. M and C show flux of M-solute and carbon atoms to the precipitate.

intermediate control is discussed in the final part of this section.

2.2. M-Solute diffusion control of growth

An M-concentration gradient cannot form in front of the advancing cell boundary during discontinuous precipitation or else a continuous growth mechanism would result. Diffusion of M (D_{BM}) therefore takes place within the boundary and the resultant concentration profile within the boundary plane is approximately as shown in Fig. 2. This profile is also left in the matrix (α) in the wake of the cell boundary. Initially, sufficient carbon is present at the growth front so that the matrix carbon diffusion is assumed infinitely fast. Balancing the M diffusing to the $M_{23}C_6$ with the M forming the $M_{23}C_6$ and assuming the convenient triangular concentration profile, we obtain

$$\pi r_p^2 C_M^\theta = \pi r_p^2 C_M^\alpha + \int_{r_p}^{(D_{BM}dt)^{1/2}} 2\pi r \Delta C_{(r)} dr \quad (1)$$

where the concentration within the boundary at distance r is given by

$$\Delta C_{(r)} = (C_M^\alpha - C_M^{\alpha\theta}) \frac{r_p + (D_{BM}dt)^{1/2} - r}{(D_{BM}dt)^{1/2}} \quad (2)$$

C_M is the concentration of solute M in the matrix (suffix α), in the $M_{23}C_6$ precipitate (suffix θ) and the matrix–$M_{23}C_6$ equilibrium at the interface (suffix $\alpha\theta$). r is the distance from the centre of the $M_{23}C_6$ rod and r_p is the radius of the rod. $(D_{BM}dt)^{1/2}$ is the extent of the solute catchment area where D_{BM} is the solute boundary diffusivity and dt is the time for the boundary to pass a point in the receding grain. V_b is the velocity of the migrating boundary so that $V_b = \delta/dt$ where δ is the width of the boundary. This reduces to

$$\frac{r_p^3}{6(D_{BM}dt)^{1/2}} + \frac{r_p^2}{2}\left(\frac{C_M^\theta - C_M^\alpha}{C_M^\alpha - C_M^{\alpha\theta}} + 1\right) - \frac{(D_{BM}dt)^{1/2}}{2} r_p - \frac{D_{BM}dt}{6} = 0 \quad (3)$$

2.3. Carbon volume diffusion control of growth

The second limiting factor in discontinuous precipitation is carbon supply from the matrix. Due to rapid

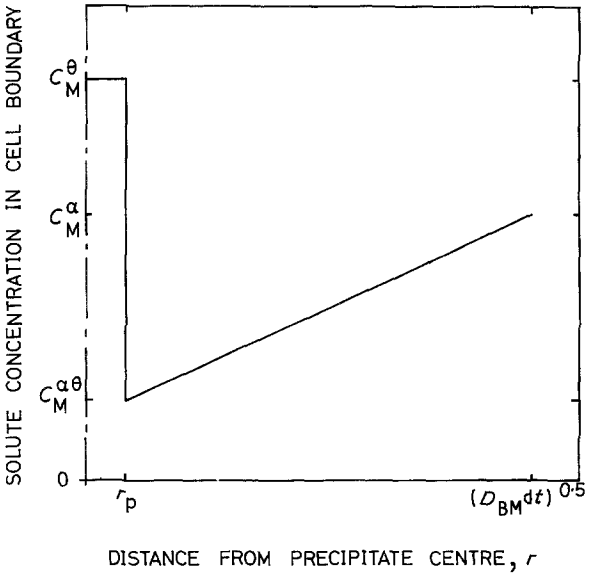

Figure 2 Theoretical solute-M concentration at the advancing boundary of discontinuous precipitation.

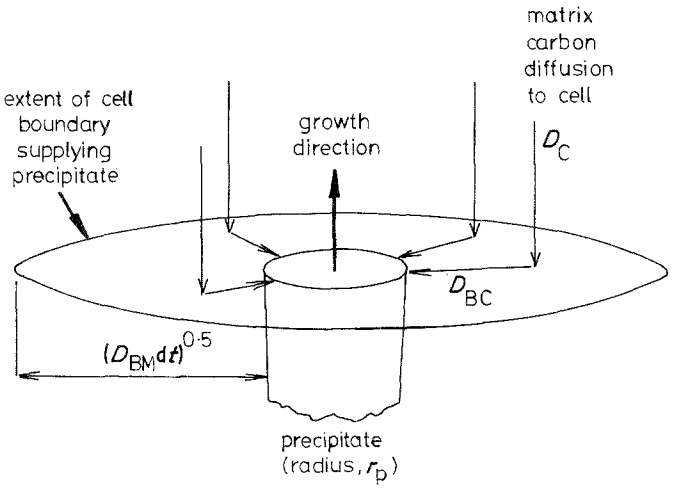

Figure 3 Collector-base model supplying carbon to discontinuous precipitate rod.

diffusion of M-solute along the boundary, rapid growth rates occur which induce carbon concentration gradients perpendicular to the boundary. The boundary diffusion of carbon, D_{BC}, will be extremely fast and may be assumed infinite when compared to that of M. The supply of carbon follows the collector-plate model displayed in Fig. 3. The amount of carbon reaching a catchment area A_v on the boundary to supply the growing $M_{23}C_6$ rod is given by a treatment similar to that of Aaron and Aaronson [4],

$$\frac{dm}{dt} = A_v D_c \frac{d}{ds}[C_c(s, t)]_s \quad (4)$$

where the concentration of carbon perpendicular to the cell boundary at distance s and time t is derived from

$$C_c(s, t) = (C_c^\alpha - C_c^{\alpha\theta})\varrho_c^\alpha \operatorname{erf}\left(\frac{s}{2D_c t}\right) + C_c^{\alpha\theta}\varrho_c^\alpha \quad (5)$$

where C_c^α and $C_c^{\alpha\theta}$ are the carbon concentrations in the matrix at $t = 0$ and in equilibrium at the matrix–$M_{23}C_6$ interface, respectively and ϱ_c^α = partial molar density of carbon in solution. Differentiating,

$$\left(\frac{dC_c}{ds}\right)_{s=0} = \left[\frac{(C_c^\alpha - C_c^{\alpha\theta})\varrho_c^\alpha}{(\pi D_c t)^{1/2}} \exp\left(\frac{-s^2}{4D_c t}\right)\right]_{s=0} \quad (6)$$

Therefore

$$\frac{dm}{dt} = \frac{A_v D_c^{1/2}}{\pi^{1/2} t^{1/2}}(C_c^\alpha - C_c^{\alpha\theta})\varrho_c^\alpha \quad (7)$$

This carbon produces $M_{23}C_6$ carbide according to

$$\frac{dm}{dt} = \left(\frac{dm}{dv}\right)\left(\frac{dv}{dt}\right) \quad (8)$$

where v = volume of carbide. The increase in density of carbon in forming carbide is

$$\frac{dm}{dv} = (C_c^\theta - C_{c(s)}^{\alpha\theta})\varrho_c^\alpha \quad (9)$$

The increase in volume of carbide with time is

$$\frac{dv}{dt} = \pi r_p^2 V_b \quad (10)$$

and r_p = radius of $M_{23}C_6$ rod. Substituting in Equation (8),

$$V_b = \frac{A_v D_c^{1/2}}{\pi^{3/2} r_p^2}\left(\frac{C_c^\alpha - C_c^{\alpha\theta}}{C_c^\theta - C_{c(s)}^{\alpha\theta}}\right) t^{-1/2} \quad (11)$$

2.4. Intermediate control

2.4.1. Introduction

Since complete growth control by the diffusion of either M or carbon relies on infinitely fast diffusion of the other, then real situations must lie somewhere between. A combination of the two cases is proposed where the equilibrium concentrations of solute M and carbon at the matrix–$M_{23}C_6$ interface are dictated by the solubility equation

$$(C_M^{\alpha\theta})^{23/6} C_c^{\alpha\theta} = \exp\left(\frac{-\Delta H}{RT} + K\right) \quad (12)$$

where K is a constant. The extremely high boundary diffusivity of carbon relative to M is still assumed so as to extend the equilibrium carbon level along the cell boundary.

It is assumed that growth control changes from one case to the other according to the boundary velocity (see Fig. 4) as will now be explained.

2.4.2. Limiting boundary velocities of discontinuous growth

The start of growth is typified by very thin $M_{23}C_6$ rods close together which is indicative of fast boundary motion. This stage is controlled by M-solute diffusion (Equation 3) where the initial uniform distribution of both M and carbon favours a ready supply of carbon. Here the equilibrium level of M at the precipitate is given by the solubility relation (Equation 12) with the carbon concentration equal to that of the general matrix, C_c. The starting and therefore maximum boundary velocity V_{max} is dependent upon

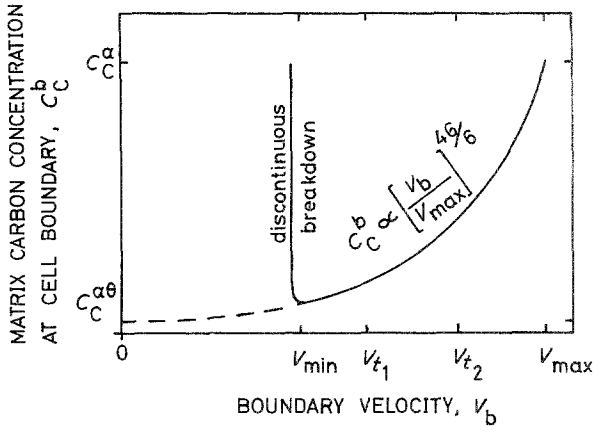

Figure 4 Carbon concentrations at cell boundary during discontinuous cell growth. Time $t_2 > t_1 > 0$.

the nucleation characteristics of the boundary and is obtained from

$$V_{max} = \frac{\text{Boundary thickness}}{\text{Time for boundary to traverse thickness}} = \frac{\delta}{dt}$$

and Fig. 2 shows the initial interparticle spacing

$$r_{ip} = (D_{BM}\,dt)^{1/2}$$

so

$$V_{max} = \frac{D_{BM}\delta}{r_{ip}^2} \quad (13)$$

The minimum boundary velocity is the velocity reached when a breakdown to continuous precipitate growth occurs. This is due to the creation of an M-solute concentration gradient immediately in front of the advancing cell boundary. This happens when the boundary velocity becomes "slower" than M-volume diffusion in the matrix, i.e. when a solute differential is set up across the atom planes parallel to the cell boundary in the receding grain:

$$\text{Minimum boundary velocity} = \frac{\text{Interplanar spacing (receding grain), } a}{\text{Time for mean diffusion over interplanar spacing}}$$

If mean diffusion distance $= (D_M t_a)^{1/2}$, then time for diffusion over interplanar distance, $t_a = a^2/D_M$; hence

$$\text{Minimum boundary velocity} = D_M/a \quad (14)$$

A rapid degeneration of discontinuous to continuous precipitate growth below this velocity is caused by a depletion of M-solute ahead of the advancing boundary.

2.4.3. Relationship between carbon and M-solute growth control

The balance of carbon and M-solute control of growth is dependent upon the carbon concentration C_c^b at the advancing cell boundary. This is linked to the $M_{23}C_6$–boundary interface M-solute concentration by the solubility relation (Equation 12) so that $C_c^b \propto (C_M)^{-23/6}$. C_c^b varies between the limiting boundary velocities, i.e. from the initial supersaturated matrix concentration C_c^α at maximum boundary velocity to $C_c^{\alpha\theta}$ at minimum velocity (see Fig. 4). The lower carbon concentration $C_c^{\alpha\theta}$ is obtained from the Equation 12 with the M-solute concentration C_M equal to the initial supersaturated matrix concentration C_M^α. This M-solute concentration is that of the receding grain matrix which by definition is unaltered throughout discontinuous growth.

During discontinuous cell growth, the M-solute concentration at the $M_{23}C_6$–boundary interface C_M is dictated by the quantity of M-solute diffusing to the $M_{23}C_6$ from the cell-boundary solute catchment area. A faster advancing cell boundary permits diffusion over a shorter distance so that less M-solute arrives at the $M_{23}C_6$ from a particular boundary direction. Considering the solute catchment area, therefore, the enforced concentration C_M will be a function of the square of the diffusion distance, so $C_M \propto 1/V_b^2$ and

$$C_c^b \propto V_b^{46/6}$$

The relationship of carbon concentration to the cell boundary velocity displayed in Fig. 4 is therefore given by

$$C_c^b = C_c^{\alpha\theta} + (C_c^\alpha - C_c^{\alpha\theta})\left(\frac{V_b}{V_{max}}\right)^{46/6} \quad (15)$$

The area on the cell boundary supplying carbon to an individual $M_{23}C_6$ rod is defined by the extent of M-solute boundary diffusion $(D_{BM}\,dt)^{1/2}$. This is shown diagramatically in Fig. 3, where carbon in the adjacent boundary follows the transport of M-solute to neighbouring rods.

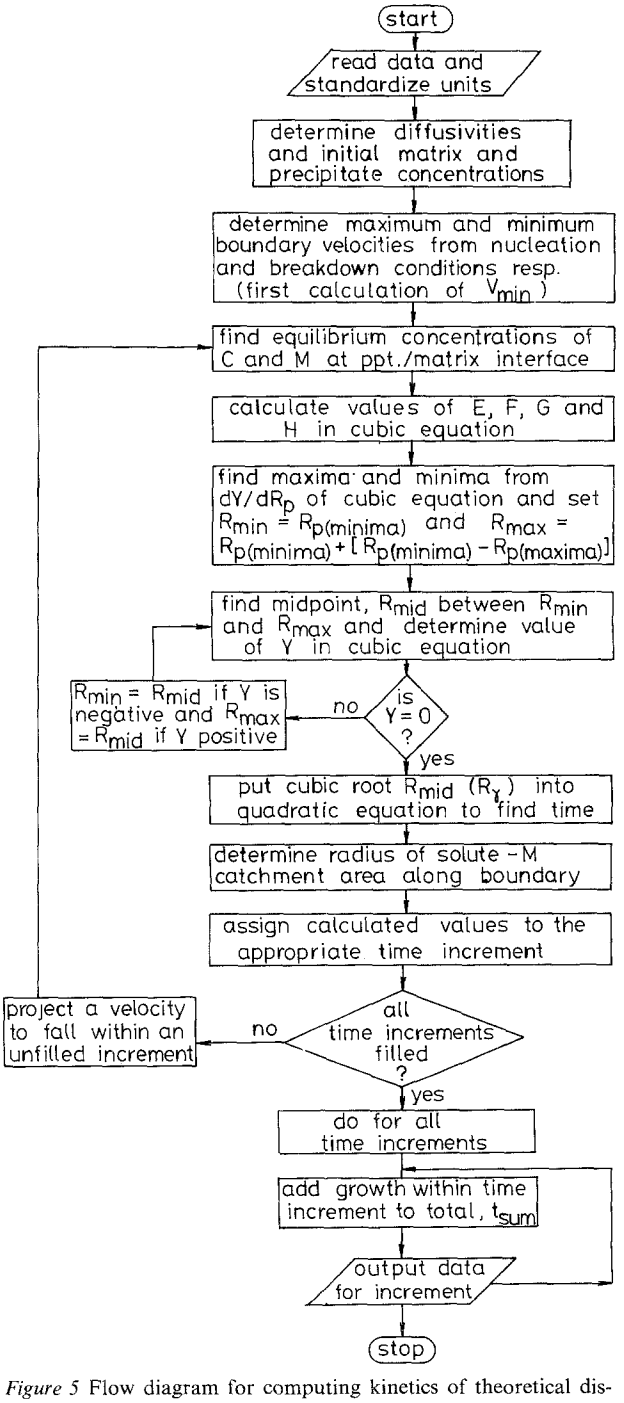

Figure 5 Flow diagram for computing kinetics of theoretical discontinuous precipitation.

2.5. Computation of discontinuous growth kinetics

The objective is to predict the variation of cell depth (boundary migration) and $M_{23}C_6$ rod diameter with growth time. The growth of discontinuous precipitates has been shown to be defined by two types of equation: Equation 11 applies to the migrating grain boundary and originates from carbon control. The second defining relation, Equation 3, is from control of the $M_{23}C_6$ rod diameter by M-solute boundary diffusion. This cubic equation is solved by consideration of its three roots (see Appendix). The two equations are connected by Equation 15 which describes the equilibrium carbon concentration at the matrix–$M_{23}C_6$ interface and boundary as a function of boundary velocity.

Mathematical integration of the growth velocity V_b is made inconceivable by its interrelation with nearly all the terms in the equations (note that dt, $C_c^{\alpha\theta}$ and $C_M^{\alpha\theta}$ depend on V_b). A computer program is therefore used to determine the growth kinetics by integrating numerically. The flow diagram is given in Fig. 5. The change in cell growth velocity with time is of the form shown in Fig. 6. The program is based on determining boundary velocities within equal time-increments, computed from the time when discontinuous precipitation breaks down, i.e. when M-solute can diffuse into the boundary from the receding grain. Growth distances can then be derived by adding the areas in the columns of the histograms produced. Accuracy may be optimized by increasing the number of time increments until negligible change in results is obtained. Typical input is given in Table I and graphical output in Figs 7a and b. Theoretical growth kinetics are more conveniently summarized in diagrammatical form as in Fig. 8, which is a scaled section of the growing $M_{23}C_6$ rod and solute catchment range with lengths attained after various times.

2.5.1. Theoretical results

The results in Fig. 7 and 8 are determined for the maximum possible growth distance, which occurs when (0 0 1) planes in the receding grain are parallel to the advancing cell boundary. In reality, growth terminates at a much earlier stage because of more closely packed planes being parallel to the advancing boundary as a result of the alloy processing history. The growth against time graph at 700° C of Fig. 7a shows that the depth of cell increases almost proportionally with time. This follows an initial rapid period of growth which is the result of a ready supply of carbon to the cell as a carbon concentration profile is set up in the receding grain matrix. Once established, a more restricted and constant amount of carbon is diffused down the concentration profile to the cell boundary.

At the end of discontinuous precipitation the curve deviates sharply to the horizontal, since the continuous growth mechanism which takes over occurs on a static boundary. Fig. 7b shows how the $M_{23}C_6$ rod radius and the associated extent of solute catch-

TABLE I Input data

Diffusion data for solute M in matrix (chromium in Inconel-600 [5]): $D_0 = 1.60\,cm^2\,sec^{-1}$, $Q = 66.1\,kcal\,mol^{-1}$ ($277\,kJ\,mol^{-1}$).

Diffusion data for solute M along grain boundary (chromium in Inconel-600 [5]: $D_0 = 4.20 \times 10^8\,cm^3\,sec^{-1}$, $Q = 42.8\,kcal\,mol^{-1}$ ($179\,kJ\,mol^{-1}$).

Diffusion data for carbon in matrix (nickel + 5% chromium [6]): $D_0 = 0.4\,cm^2\,sec^{-1}$, $Q = 37.5\,kcal\,mol^{-1}$ ($157\,kJ\,mol^{-1}$).

Grain-boundary diffusion channel = 0.15 nm [7].

Matrix interplanar spacing = 0.356 nm [8].

Grain-boundary area per unit volume of matrix = $71 \times 10^{-6}\,nm^2\,nm^{-3}$ [1].

Distance between discontinuous precipitate nuclei (observed after 700° C ageing) along grain boundary = 20 nm [1].

Carbon concentration in matrix (solution-treated) = 0.08 at % [1].

Matrix concentration: M(Cr + Fe) = 22.68 at %, Ti = 2.33 at %, Al = 1.4 at %, Si = 0.36 at %, Ni = balance [1].

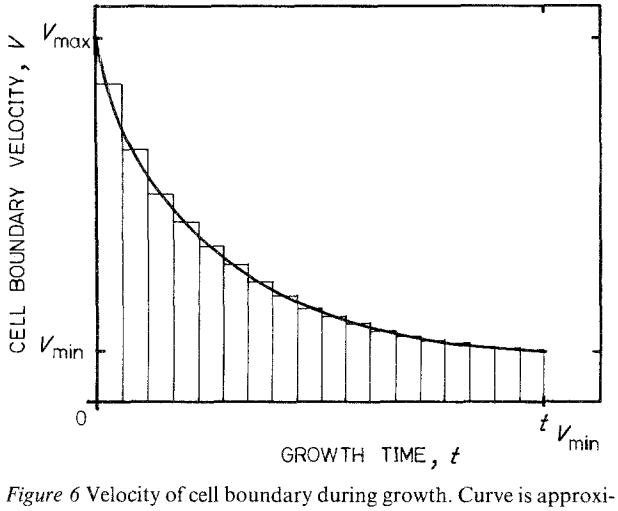

Figure 6 Velocity of cell boundary during growth. Curve is approximated to a histogram in computer program.

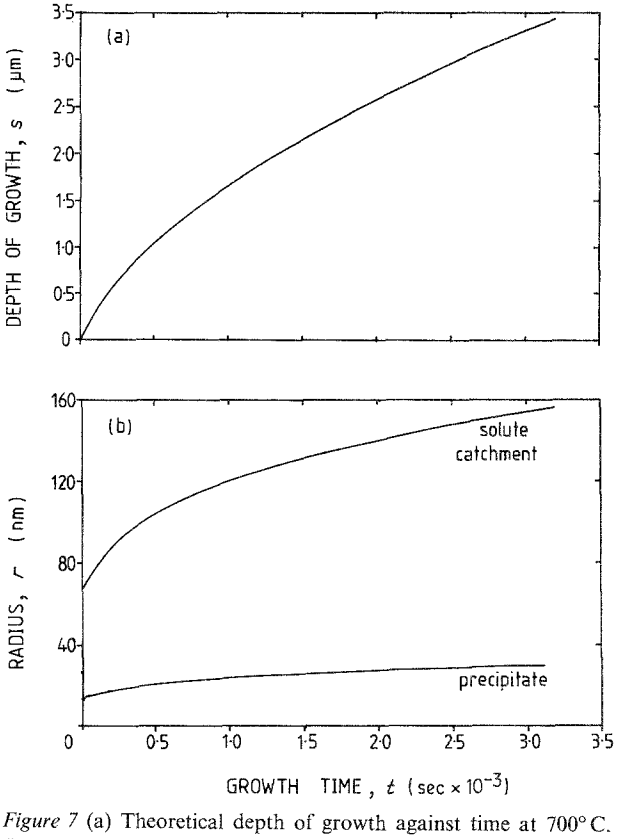

Figure 7 (a) Theoretical depth of growth against time at 700° C. (b) Theoretical radius of $M_{23}C_6$ rod and solute catchment area on cell boundary against time at 700° C.

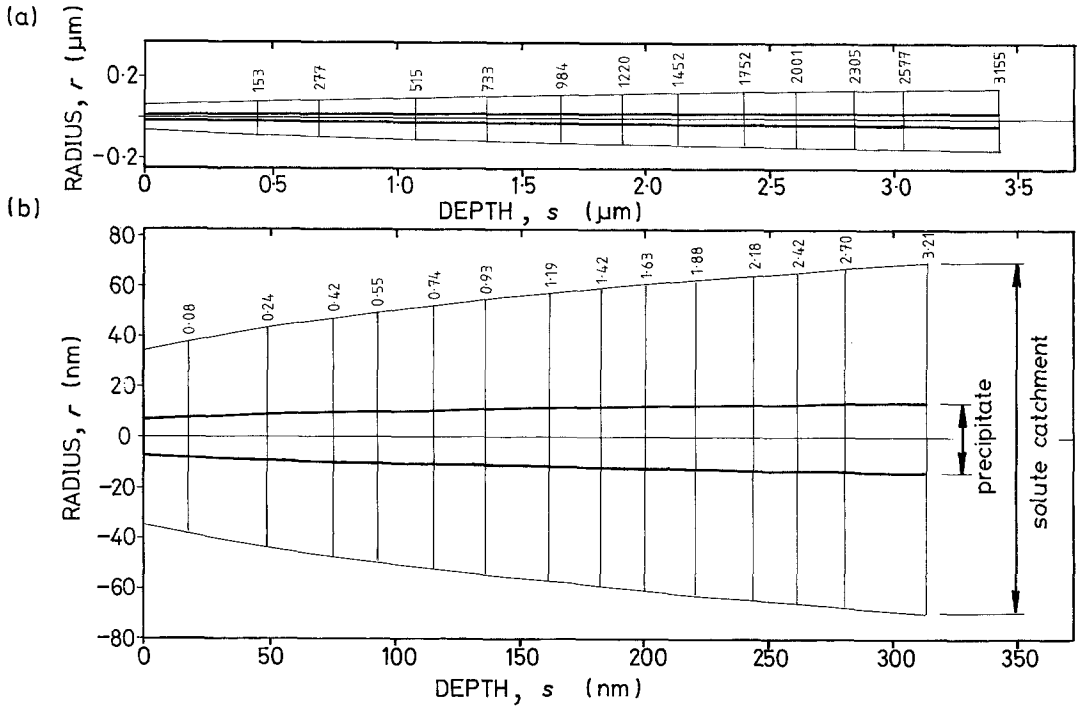

Figure 8 Comparison of discontinuous growth at (a) 700° C and (b) 850° C. Time of precipitate growth is indicated in seconds.

ment area expand quickly from the nucleus. This must simultaneously cause the extinction of a large number of $M_{23}C_6$ rods growing from smaller nuclei. The dimensions then stabilize with a ratio of solute catchment radius to rod radius of approximately 5 : 1.

Growth processes at 700 and 850° C are compared in Fig. 8 (note different scales). The theory predicts a much faster growth rate at 850° C together with larger radii of $M_{23}C_6$ rod and solute catchment area. The cell growth is, however, terminated early since the high diffusivity which aids discontinuous precipitation also causes a quicker breakdown to continuous growth.

The predicted shapes of precipitate in Fig. 8 match the experimental observations. The typical cell shown in Fig. 1a exhibits average $M_{23}C_6$ rod precipitates similar in proportion when it is considered they have only reached a length of 875 nm. Although a number are undoubtedly cut by the foil surface, it seems that some $M_{23}C_6$ rods have been stunted in growth, particularly near the base of the cell. This is in agreement with the predicted maximum growth rates occurring early in growth. It is thought that the distinct widening of a few of the rods along their length is due to the takeover of solute catchment areas on the boundary from those rods becoming extinct.

3. Observation and measurement of discontinuous precipitation of $M_{23}C_6$ in Nimonic 80A

3.1. Experimental techniques

Nimonic 80A (Wiggin Alloys Ltd) was extruded and hot-rolled to 15 mm diameter round bar. The manufacturer's analysis together with the specified composition range and maximum values are given in Table II. The material was solution-annealed at 1080° C for 2 h and water-quenched. It was then cut into 20 mm lengths and two 0.5 mm thick transverse slices were spark-eroded from each. These were subsequently aged together with the corresponding length of bar. Different ageing treatments were applied at either 700 or 850° C for periods of up to 4 h. A heating-to-temperature correction was added to the ageing time, based on the reverse of the cooling correction proposed by Williams *et al.* [9]. This amounted to 90 sec at 700° C and 112 sec at 850° C.

3 mm diameter foils were prepared from the slices of bar using a standard electrochemical polishing technique. The electrolyte was 20% perchloric acid in ethanol (both Analar) at − 10° C using a voltage of 15 V with an approximate current of 80 mA.

Transmission electron microscopy (TEM) was conducted at 100 kV accelerating voltage on a Jeol JEM-100CX STEMMA machine. A specimen holder incorporating a double stage-tilt mechanism was used so that clockwise and counter-clockwise tilts of 60° could be made about two axes perpendicular to each other.

Details were recorded from all grain boundaries visible in a thin foil during observation by TEM. Discontinuous precipitate images were photographed from clockwise and counter-clockwise rotations of both tilt stages to obtain a minimum 45° angular difference. Magnifications ranged from 10 000 to 33 000 according to precipitate size. To achieve a meaningful statistical analysis at least 300 negatives were taken for each sample ageing treatment. Measurements were taken direct from negatives to eliminate excessive printing and the accompanying errors such as paper stretching and loss of definition. The following were recorded for each viewing direction of a cell,

TABLE II Alloy composition (and specification) (wt %)

C = 0.065 (0.100 max.)	Si = 0.36 (1.00 max.)
Cr = 20.2 (18.0 to 21.0)	Mn = 0.60 (1.00 max.)
Co = 0.15 (2.0 max.)	Fe = 1.33 (3.00 max.)
Ti = 2.33 (1.80 to 2.70)	Cu = less than 0.05 (0.2 max.)
Al = 1.40 (1.00 to 1.80)	Ni = balance

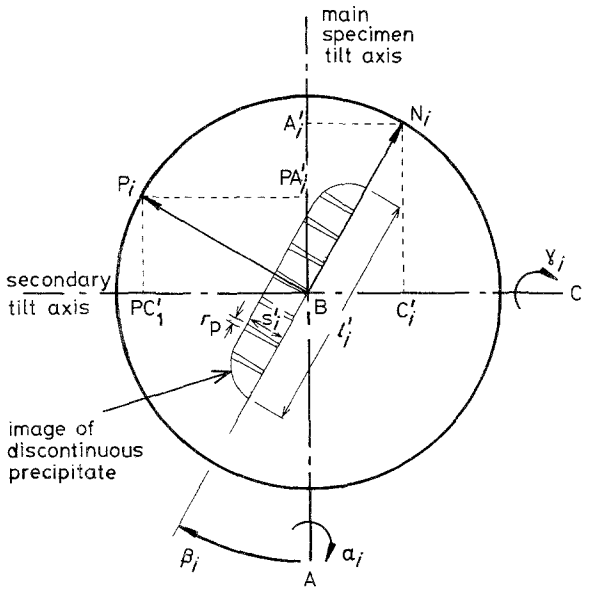

Figure 9 TEM image measurements for determination of precipitate growth dimensions.

as displayed in Fig. 9:

(a) Apparent length of cell along grain boundary, l;
(b) apparent depth of cell, s';
(c) radius of $M_{23}C_6$ rod at advancing cell boundary, r_p;
(d) specimen rotation about main axis, α;
(e) specimen rotation about secondary axis, γ; and
(f) angle between perpendicular to projected precipitate growth direction and the main axis, β.

Information was stored and analysed on a main-frame computer. In addition, for the samples given a short ageing treatment (4 min), grain misorientations and precipitate growth directions were determined using a recently developed technique [10].

3.2. True precipitate size determination

True precipitate dimensions are determined by coordinate geometry in a similar procedure to the grain misorientation and precipitate direction technique [10]. A projection of the precipitate direction P_i is assigned coordinates (PA_i', PB_i', PC_i') from the image negative. Fig. 9 shows these to be [cos (β_i − 90°), 0, sin (β_i − 90)] where the suffix i designates either the first or second precipitate image. The coordinates (A_i', B_i', C_i') of the normal to the plane N_i in which the true precipitate lies are (cos β_i, 0, sin β_i).

The two sets of coordinates are now standardized to a common coordinate base which is conveniently taken as the zero specimen-tilt position. Firstly, the main axis tilt of α_i is returned to zero tilt by rotating by α_i in its opposite sense using a transformation matrix:

$$\begin{bmatrix} 1 & 0 & 0 \\ 0 & \sin\alpha_i & 0 \\ 0 & 0 & \cos\alpha_i \end{bmatrix}$$

The standardization is completed by a similar adjustment of γ_i about the secondary axis, i.e. following the transformation matrix

$$\begin{bmatrix} \cos\gamma_i & \sin\gamma_i & 0 \\ -\sin\gamma_i & \cos\gamma_i & 0 \\ 0 & 0 & 1 \end{bmatrix}$$

The true precipitate direction is then obtained from the intersection of the two planes defined by the resulting normals (A_1, B_1, C_1) and (A_2, B_2, C_2), i.e.

$$PA_t = B_1C_2 - B_2C_1$$
$$PB_t = C_1A_2 - C_2A_1$$
$$PC_t = A_1B_2 - A_2B_1$$

The angle θ_i between the true precipitate direction and the projected direction on the image i is given by the standard formula

$$\cos\theta_i = \frac{PA_t PA_i + PB_t PB_i + PC_t PC_i}{(PA_t^2 + PB_t^2 + PC_t^2)^{1/2}(PA_i^2 + PB_i^2 + PC_i^2)^{1/2}}$$

and the true depth of cell is therefore

$$s = s_i'/\cos\theta_i$$

The true length l of cell section along the grain boundary as cut by the foil plane is determined from the projected length on the image:

$$l = l_i'/\cos\phi_i$$

where ϕ_i is the angle separating the grain-boundary image (i.e. normal N_i) from the resulting position after standardization, i.e. (A_i, B_i, C_i), so that

$$\cos\phi_i = \frac{A_i\cos\beta_i + C_i\sin\beta_i}{(A_i^2 + B_i^2 + C_i^2)^{1/2}}$$

3.3. Experimental results

The large amount of data necessary for a meaningful size analysis of each ageing treatment limited the examination to the following samples:

(a) 4 min at 700° C,
(b) 16 min at 700° C,
(c) 4 h at 700° C,
(d) 4 min at 850° C and
(e) 2 h at 850° C.

The measured cell dimensions are presented as frequency against size-range histograms in Figs 10, 11 and 12 respectively for true length of cell section along the grain boundary (l), true depth of cell growth (s) and growth radius of $M_{23}C_6$ rods (r_p). The series of histograms in Figs 11 and 12 are summarized in Figs 13 and 14 and Table III.

3.3.1. Length of cell section along grain boundary, l

The area of grain boundary occupied by a single cell is irregularly shaped. The measurement of an arbitrary length of cell section, such as in the TEM, therefore provides only an indirect comparison of the areas of discontinuous precipitation between different samples.

The series of histograms in Fig. 10 for ageing at 700° C infer that the cell sections increase in length with time. After 4 min the distribution peaks at 0.5 μm

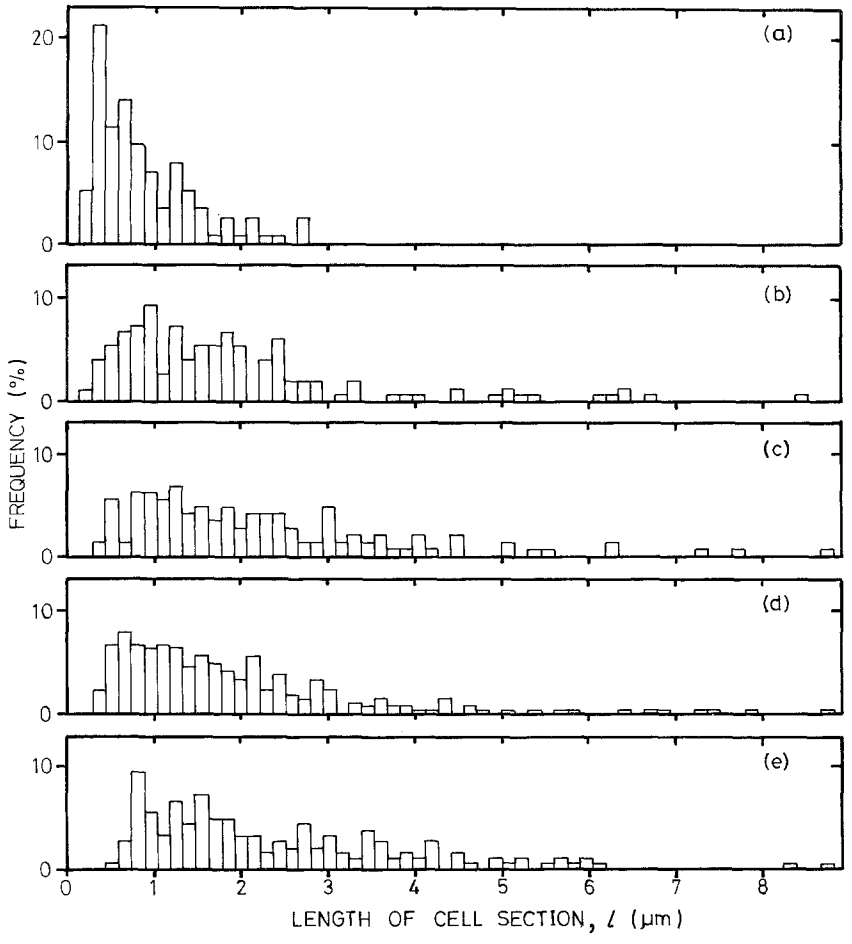

Figure 10 Histograms of length of cell section measured along grain boundary at various ageing treatments. (a) 4 min at 700° C, (b) 16 min at 700° C, (c) 4 h at 700° C, (d) 4 min at 850° C, (e) 2 h at 850° C.

and the tail ends at 2.5 μm. After 16 min the peak is flattened and increased to about 1 μm, whilst the tail is considerably extended. A 4 h age results in an even flatter peak and a longer, thicker tail. This is due to the merging of adjacent cell sections (which are likely to be part of the same cell anyway) as they grow further into a grain and can envelop pinning points, such as primary particles, existing on the grain boundary.

The distribution of cell sections after 4 h at 700° C is similar to that achieved after both 4 min and 2 h ageing at 850° C. This reflects the faster growth of discontinuous precipitates at 850° C and possibly also a similar siting of the discontinuous cells, even though there is a significant increase in continuous grain-boundary precipitation at 850° C.

3.3.2. Discontinuous precipitate growth

The progress of discontinuous growth during ageing at 700° C is followed by the histograms (a) to (c) in Figs 11 and 12.

TABLE III Summary of data on grain-boundary precipitation in aged specimens

Property	Specimen No.				
	1	2	3	4	5
Ageing temperature (° C)	700	700	700	850	850
Ageing time	4 min	16 min	4 h	4 min	2 h
Average precipitate radius (nm)	10.5	12.7	20.1	18.6	36.4
Spread	3.53	4.24	12.11	10.21	23.06
Average precipitate depth (nm)	258.2	306.5	514.4	174.8	183.9
Spread	182.2	276.3	418.4	168.8	145.8

Fig. 11 shows that the distribution of cell depths gradually changes from a peak around 100 nm (with a long thin tail) after 4 min at 700° C, to a broad distribution after 4 h. Fig. 12 shows that there is a corresponding change in radius of $M_{23}C_6$ rod at the advancing cell boundary from a narrow peak around 10 nm to a broad peak around 20 nm. Different discontinuous precipitate cells therefore appear to have significantly different rates of growth and to stop growing after different periods of ageing.

Histograms (d) and (e) in Figs 11 and 12 are for growth at 850° C. Here discontinuous growth proves to be almost complete after 4 min ageing, since subsequent ageing to 2 h increases the depth of growth very little. The radius of the $M_{23}C_6$ rod is seen to double during this time. This is the result of continuous $M_{23}C_6$ precipitation taking over from the discontinuous reaction which causes enlargement of the end of the $M_{23}C_6$ rod along the cell boundary.

The variations of growth dimensions are plotted in Figs 13 and 14 against a logarithmic scale of ageing time. The growth attained by discontinuous precipitates at 700° C is much greater and more variable than at 850° C. Also, the growth radius of the $M_{23}C_6$ rod is correspondingly smaller at 700° C.

3.3.3. Grain orientations and precipitate growth directions

Grain-boundary mismatch and precipitate growth directions are identified for all discontinuous precipitates measured in the samples aged for 4 min at 700 and 850° C. All data are normalized with respect to the three-dimensional symmetry of the cubic (f c c) crystal

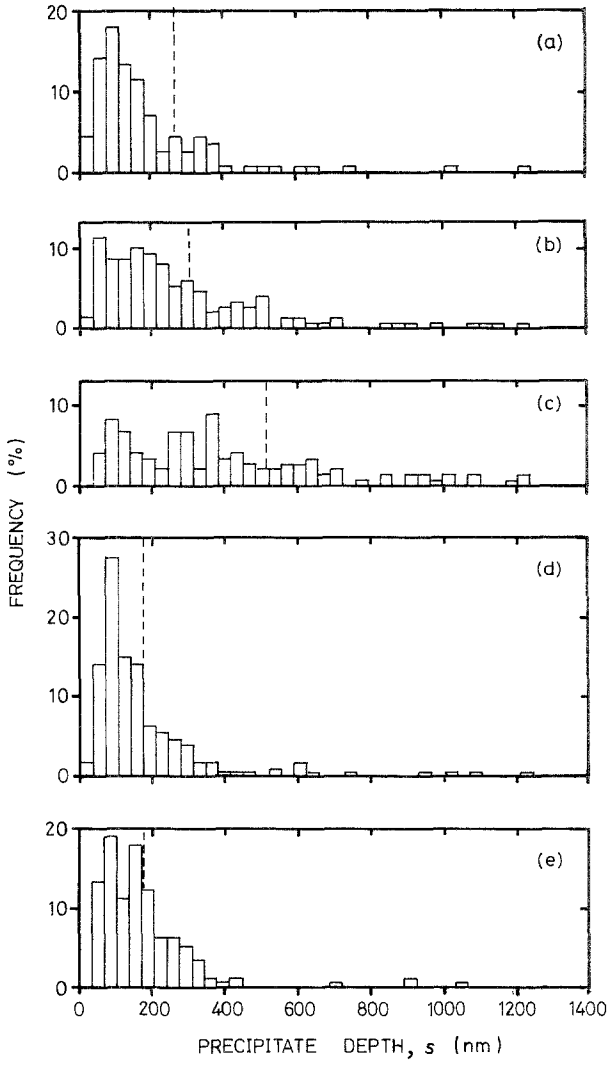

Figure 11 Histograms of measured depths of discontinuous precipitation at various ageing treatments: (a) 4 min at 700° C, (b) 16 min at 700° C, (c) 4 h at 700° C, (d) 4 min at 850° C, (e) 2 h at 850° C. Average depth shown by dotted line.

structure of both matrix and $M_{23}C_6$ carbide precipitate phases.

No preferred grain misorientations across grain boundaries containing discontinuous precipitation are evident in either of the samples studied.

The $M_{23}C_6$ rod growth directions at 850° C shown in the standard triangles of Fig. 15 reveal a tendency towards $\langle 1\,1\,0 \rangle$ growth relative to the advancing cell. In the receding grain, directions are random. No preferred growth direction occurs at 700° C relative to either grain.

4. Comparison of theory and experiment

The proposed hybrid growth of discontinuous precipitates via boundary M-solute and carbon volume diffusion control has predicted $M_{23}C_6$ rod morphologies similar to those observed in practice. Unfortunately, the measurements of discontinuous precipitation cannot be directly related to growth kinetics since they include an unknown number of cells which had ceased growing earlier in the ageing treatment. Average experimental measurements are compared with the theoretical growth of a single discontinuous precipitate at 700° C in Fig. 16. It should be emphasized that in practice the receding grains would be randomly

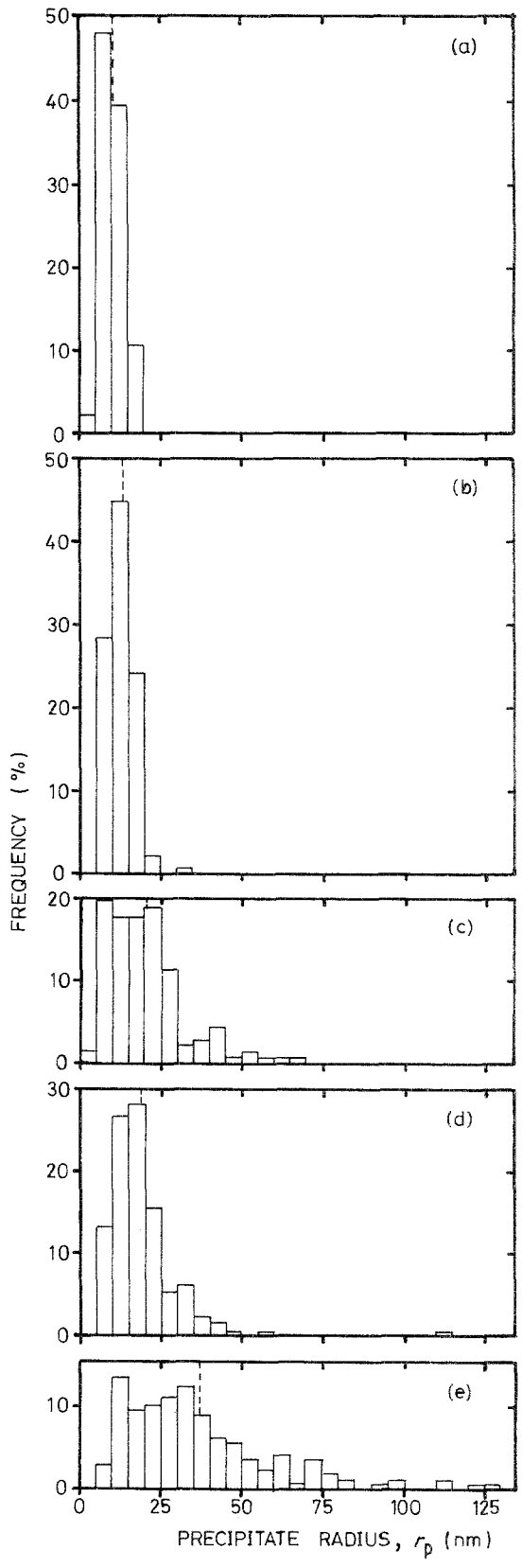

Figure 12 Histograms of radius $M_{23}C_6$ rod measured at advancing cell boundary at various ageing treatments: (a) 4 min at 700° C, (b) 16 min at 700° C, (c) 4 h at 700° C, (d) 4 min at 850° C, (e) 2 h at 850° C.

orientated, and so theoretical discontinuous growth termination would mainly occur before even the first cut-off case shown of the receding grain with a (2 2 1) plane parallel to the cell boundary. This is much earlier than observed in practice, where growth is shown to continue beyond at least 1050 sec ageing and possibly beyond 14 500 sec ageing (seen better in Fig. 13). Since more cells terminate growth as ageing

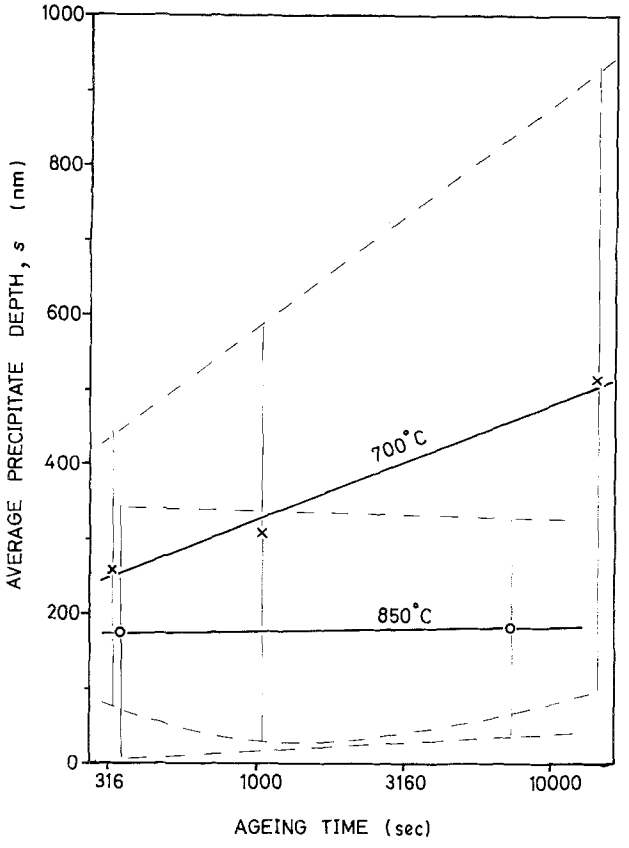

Figure 13 Average depth of discontinuous precipitation against time (logarithmic scale) at 700 and 850° C. Standard deviation limits are shown.

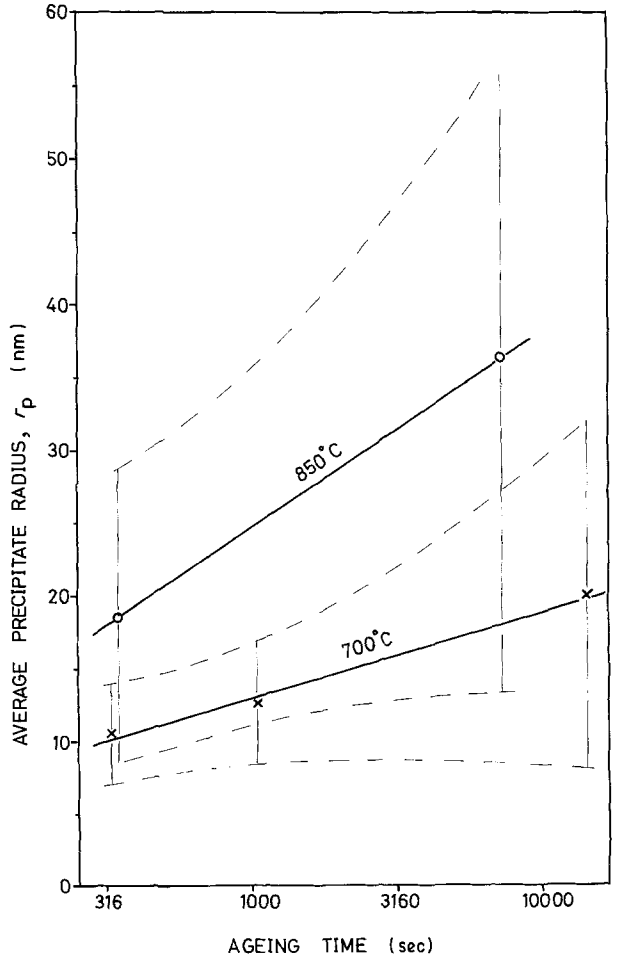

Figure 14 Average radius of $M_{23}C_6$ rod measured at advancing cell boundary against time (logarithmic scale) at 700 and 850° C. Standard deviation limits are shown.

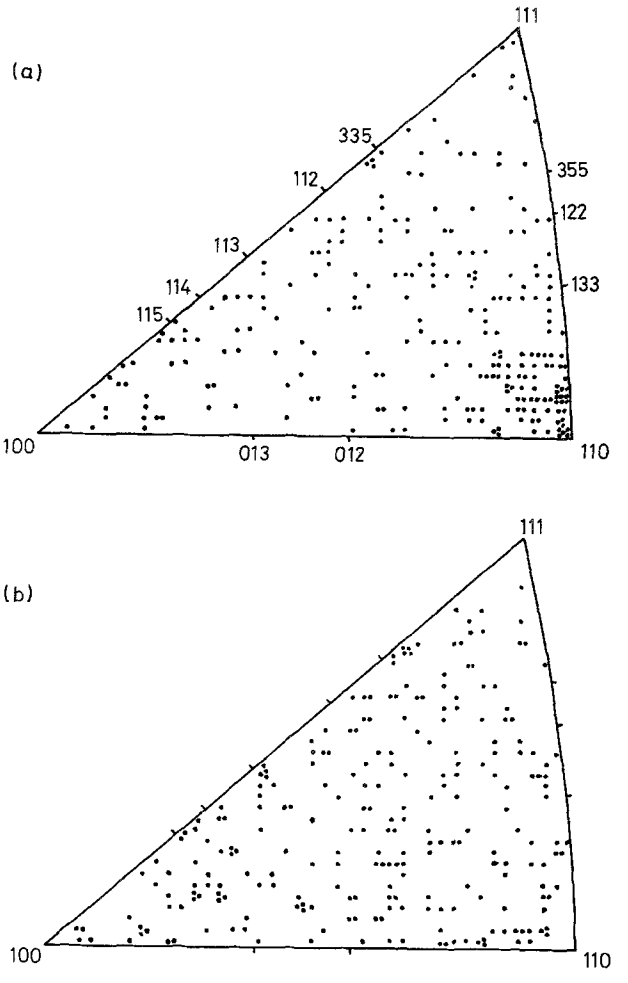

Figure 15 Standard triangles showing precipitate growth directions after ageing at 850° C for 4 min: (a) in host grain, (b) into receding grain.

time increases, the greater deviation of the average measured cell from the theoretical case with time is to be expected. At the shorter ageing times, some individual cells are recorded (Fig. 11a) which match theoretical depths of growth but overall, the average measured cell growth is slower than predicted.

Fig. 17 compares the theoretical and average measured radius of $M_{23}C_6$ at the advancing cell boundary with increase in cell depth at 700° C. The influence of terminated discontinuous growth is evident in the steep rise in measured radius.

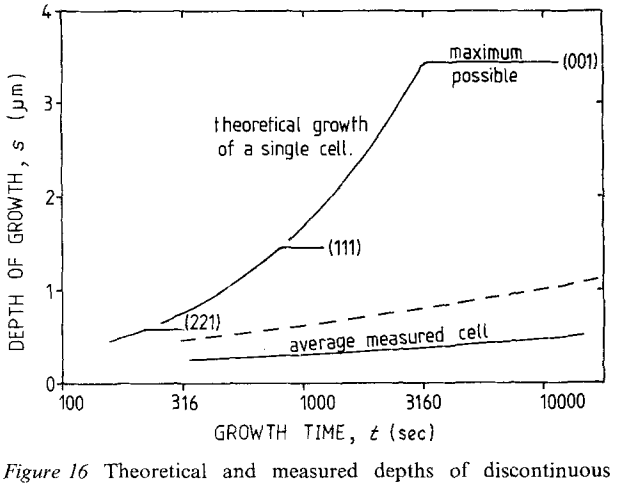

Figure 16 Theoretical and measured depths of discontinuous precipitate growth against ageing time at 700° C. Average measured growth includes cells which have ceased growth earlier in the ageing treatment. Dotted line shows one standard deviation.

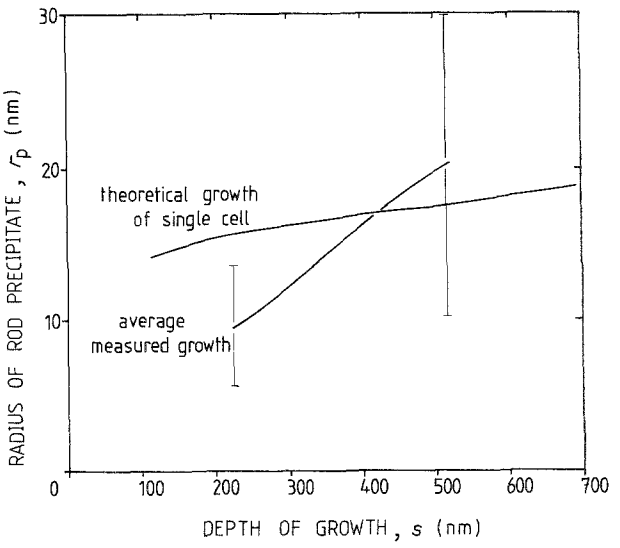

Figure 17 Theoretical and measured radius of $M_{23}C_6$ rod at advancing boundary against depth of cell. Average measured growth is distorted by extinct discontinuous cells which have converted to continuous precipitation.

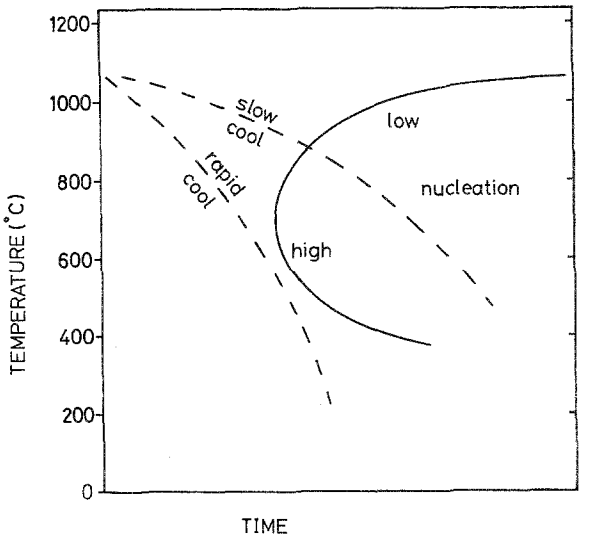

Figure 18 Temperature against nucleation time "C" curve.

Subsequent continuous growth causes $M_{23}C_6$ precipitates to grow along a static grain boundary. The shallower growths at the shorter ageing time therefore offer a better comparison of discontinuous growth. Here, experimental growths have a smaller precipitate rod radius than predicted.

The prediction of discontinuous growth at 850° C (Fig. 8b) similarly cannot be directly compared with experimental measurements (Figs 13 and 14) due to the early termination of cell growth. Growth is predicted to last merely for a few seconds and to reach a depth of less than 300 nm. Observations begin at the much later ageing time of 240 sec, when growth is shown to be complete with an average depth of 175 nm.

This rapid growth is probably why a preferred ⟨1 1 0⟩ growth direction is revealed after 4 min ageing at 850° C (Fig. 15) but not after 4 min ageing at 700° C. In the latter, the juvenile stage of growth is constrained to the initial random direction imposed by the grain boundary. The senile stages completed by the 850° C case, however, can sustain growth by deviating to an easier growth direction, i.e. presenting a lower-energy precipitate interface to the host grain matrix, and a closely knit plane of atoms to the cell boundary on to which "boundary" atoms more readily realign.

An indirect comparison of the proposed theory with experiment appears to show a consistent overestimate of discontinuous growth rate. It is possible that data used in the theoretical determinations are inaccurate. In particular, grain-boundary diffusivity is thought to be highly variable, not only between different alloys but also between grain boundaries within an alloy. Bernardini *et al.* [7] have shown that δ, the grain-boundary thickness used in the determinations of grain boundary diffusivity, may also be subject to errors of 100%. This not only affects growth rate but also the grain-boundary nucleation kinetics which provide the initiating conditions for discontinuous growth. Nucleation theory is not sufficiently advanced to predict internuclear spacings on a grain boundary, although notable progress is being made [11]. The spacing r_{ip} used in the determination is therefore an estimate from a convenient example observed in practice, and may not be truly representative. If, as suspected, this is highly variable from boundary to boundary, large discrepancies would result.

Indeed, the effect of a less densely populated grain boundary is to shorten the time of growth of discontinuous precipitates because V_{max} in Equation 13 is reduced. In the extreme, nuclei become too widely spaced to initiate discontinuous growth. This is apparent at the higher ageing temperature of 850° C, where discontinuous growth was found on 86% of the observed boundary compared to 98% at 700° C. Nucleation rates can be broadly described by "C" curves of temperature against rate, with the nose in this case being close to 700° C in Fig. 18. Hence slower cooling rates or higher ageing temperatures, so that the nose is avoided on this "C" curve, will give lower rates of nucleation. This results in larger values of r_{ip} in Equation 13 and hence shorter growth times.

Considering the difficulty in relating theory to experimental data and the influence of highly variable grain boundaries, the proposed model of discontinuous growth is feasible. It is considerably better than simplistic theories which predict a constant growth rate with time and no termination of growth. It is also more realistic than theories based on a reduced growth rate due to an increase in area of cell boundary, since this is observed to affect only the edge of a discontinuous cell.

4.1. Practical implications

Discontinuous precipitation of $M_{23}C_6$ in nickel-base superalloys is of great interest because of its deleterious effect on mechanical and chemical properties. For instance, it is reported that in Waspalloy it causes a significant decrease in high-temperature ductility [12] and in Incoloy 825, grain boundaries are sensitized to intergranular corrosion [13]. Furthermore, discontinuous precipitation has been reported to be always present in commercial alloys [14].

The results here imply that discontinuous precipitation may in the future be eliminated by controlled nucleation. Nucleation theory is approaching the stage where internuclear spacing can be predicted [11].

A crude application of nucleation theory suggests that control is possible by using high ageing temperatures (> 800° C) and avoiding rapid cooling rates. However, thin sections of the component may still be too rapidly cooled. A possible further improvement would then be a short isothermal anneal in the higher ageing temperature range (~ 900° C). Also it may help to reduce the amount of carbon available for precipitation by control of alloy composition and solution heat-treatment [15].

5. Conclusions

1. A hybrid mechanism for the growth of $M_{23}C_6$ discontinuous precipitates in nickel-base superalloys is developed which makes use of computer integration. Growth control is balanced between M-solute grain-boundary diffusion and carbon volume diffusion.

2. A method of determining the true dimensions of discontinuous precipitate sections observed in TEM is detailed.

3. Measurements of discontinuous $M_{23}C_6$ precipitates in Nimonic 80A following various times of ageing at 700 and 850° C are recorded. Termination of discontinuous growth with subsequent continuous precipitate growth is a significant feature. Discontinuous growth is found to proceed in some cases up to 4 h ageing at 700° C, but is well complete before 4 min ageing at 850° C.

4. The theoretical determinations predict morphologies similar to those observed in practice, and kinetics which although they seem to be faster than recorded show the proposed growth mechanism to be feasible.

5. The preferred discontinuous growth direction $\langle 1\,1\,0 \rangle$ relative to the advancing cell was discovered after 4 min ageing at 850° C.

6. Possible means of reducing the amount of discontinuous precipitation include the use of high ageing temperatures, slow cooling rates from solution-treatment temperatures, lowering the matrix carbon content, and raising the content of strong carbide-forming elements.

Acknowledgements

The authors wish to thank Professor I. A. Menzies for provision of facilities. They are also indebted to SERC and INCO (Europe) Ltd for the funding of this research. Special thanks are due to Dr P. J. Bridges for industrial supervision of the CASE award to W.E.V.

Appendix 1: Solution of the cubic equation describing M-solute control of growth

The three roots r_α, r_β and r_γ of Equation 3 in the text are obtained from

$$r_\alpha + r_\beta + r_\gamma = -3(D_{BM}\,dt)^{1/2}\left(\frac{C_M^\theta - C_M^\alpha}{C_M^\alpha - C_M^{\alpha\theta}} + 1\right)$$

$$r_\beta r_\gamma + r_\gamma r_\alpha + r_\alpha r_\beta = -3D_{BM}\,dt$$

$$r_\alpha r_\beta r_\gamma = (D_{BM}\,dt)^{3/2}$$

These roots are characterized by locating the maximum and minimum of the curve. Equation 3 is conveniently represented by

$$Y = er_p^3 + fr_p^2 + gr_p + h = 0$$

where

$$e = 1/6(D_{BM}\,dt)^{1/2}$$

$$f = \frac{1}{2}\left(\frac{C_M^\theta - C_M^\alpha}{C_M^\alpha - C_M^{\alpha\theta}} + 1\right)$$

$$g = -(D_{BM}\,dt)^{1/2}/2$$

$$h = -D_{BM}\,dt/6$$

Differentiating this equation,

$$\frac{dY}{dr_p} = 3er_p^2 + 2fr_p + g = 0$$

which has two roots from

$$\frac{-2f \pm (4f^2 - 12eg)^{1/2}}{6e}$$

Since the terms used in constants e, f, g and h are indisputably positive with $C_M^\theta > C_M^\alpha$ and $C_M^\alpha > C_M^{\alpha\theta}$, the value within the square root will always be greater than $2f$ since $(-12eg)$ is positive. Consequently the maximum will have a negative and the minimum a positive r_p, and due to the negative value of h the intermediate roots r_β and r_α will always be negative. The third root r_γ must be positive and is therefore the only practical solution to the cubic equation. This may be found by taking the r_p at the minimum which has negative Y and an arbitrary larger r_p which gives positive Y, and selecting intermediate values of r_p until zero Y is obtained. This is a procedure which is suited for computer programming.

References

1. W. E. VOICE, PhD thesis, Loughborough University of Technology (1982).
2. W. GUST, in Proceedings of Phase Transformations Conference, York, April 1979, Vol. 2 (Institution of Metallurgists, London) p. 27.
3. D. B. WILLIAMS and E. P. BUTLER, *Int. Metals Rev.* **3** (1981) 153.
4. H. B. AARON and H. I. AARONSON, *Acta Metall.* **16** (1968) 789.
5. D. D. PRUTHI, M. S. ANAND and R. P. AGAVWALA, *J. Nucl. Mater.* **64** (1977) 206.
6. P. L. GRUZIN, YU. A. POLIKARPOV and G. B. FEDEROV, *Fizaka Metallori Metaloredenie* **4** (1) (1957) 94.
7. J. BERNARDINI, P. GAS, E. D. HONDROS and M. P. SEAH, *Proc. R. Soc.* **A379** (1982) 159.
8. G. N. MANIAR, J. E. BRIDGE, H. M. JAMES and G. B. HEYDT, *Metall. Trans.* **1** (1970) 31.
9. T. M. WILLIAMS, A. M. STONEHAM and D. R. HARRIES, *Metal Sci.* **10** (1976) 14.
10. W. E. VOICE and R. G. FAULKNER, *J. Microsc.* **135** (1984) 241.
11. R. A. CAROLAN and R. G. FAULKNER, Metals Society Publication No. 280 (Metals Society, London, 1982) p. 22.
12. P. S. KOTVAL and H. HATWELL, *Trans. AIME* **245** (1969) 1821.
13. E. L. RAYMOND, *Corrosion* **24** (1968) 180.
14. C. Y. BARLOW and B. RALPH, *J. Mater. Sci.* **14** (1979) 2500.
15. W. E. VOICE and R. F. FAULKNER, *Met. Trans.* **16A** (1985) 511.

Received 1 October 1986
and accepted 10 April 1987